--- DRAFT 8/15/11 ---

Search for zonal flows in the edge turbulence of Alcator C-Mod

S.J. Zweben[1], J.L. Terry[2], M. Agostini[3], R. Hager[4], J. Hughes[2], J.R. Myra[5], D.C. Pace[6] and the Alcator C-Mod Group

[1]*Princeton Plasma Physics Laboratory, Princeton NJ 08540*

[2]*Massachusetts Institute of Technology, Cambridge MA 02139*

[3] *Consorzio RFX, Associazione EURATOM, I-35127, Padova Italy*

[4]*Max Planck Institute for Plasma Physics, D-85748 Garching, Germany*

[5] *Lodestar Research Corporation, 2400 Central Ave., Boulder CO 80301*

[6]*ORISE, Oak Ridge, TN 37831*

Abstract

The time-dependent radial and poloidal velocity of edge turbulence is evaluated using a 2-D time-delayed cross-correlation analysis of fast camera data from the gas puff imaging (GPI) diagnostic in Alcator C-Mod. The local poloidal velocity fluctuations are averaged over the poloidal viewing region of the GPI diagnostic and radially resolved over ±2 cm around the separatrix. The resulting poloidal velocity usually has a broadband frequency spectrum in the range ~1-20 kHz, and a radial correlation which increases at lower line-averaged density. In some cases with ICRH heating there was also a coherent poloidal velocity oscillation at 6-7 kHz, which was highly correlated with a poloidal magnetic field oscillation at the same frequency. Some of these results are at least partially similar to the GAMs and/or zonal flows described in theory and previous experiments.

1. Introduction

The velocity of edge turbulence in tokamaks is an important factor in determining the plasma parameters of the edge and scrape-off layer (SOL). The radial motion of turbulence is generally considered to be the dominant cause of edge transport [1-3], and the poloidal motion can in theory control the turbulence level *via* mean or time-dependent zonal flows [4-8]. Therefore it is important to measure both the radial and poloidal motion of turbulence in order to understand the physics of the cross-field transport in the edge and SOL of tokamaks.

The present paper describes time-resolved measurements of the radial and poloidal velocity of edge turbulence in Alcator C-Mod made using a gas puff imaging (GPI) diagnostic, which can measure edge turbulence within a radial range about ±2 cm near the outer midplane separatrix. This imaging data was taken at an upgraded speed of 391,000 frames/sec, and the 2-D cross-correlation analysis method used here is capable of resolving turbulence velocity fluctuations up to about 30 kHz.

The main goal of this paper was to search for the presence of time-dependent poloidally directed zonal flows in the GPI data by averaging the local velocity measurement over the available poloidal field of view. This goal was motivated by recent measurements of poloidal velocity fluctuations, i.e. zonal flows, in the frequency range ~5-20 kHz, as reviewed in [5-8]. Many of these measurements have been made locally within a single poloidal/toroidal region [9-19], while others have used two widely separated detectors to measure the global structure of these flows [20-26]. Various types of diagnostic techniques have also been used; for example, heavy ion beam probes in CHS [20], Langmuir

probes in T-10 [21], visible imaging in D-IIID [9], and microwave reflectometry in ASDEX Upgrade [12].

In general, two types of zonal flows have been identified: a coherent oscillations which has been identified with the theoretically-predicted geodesic acoustic mode (GAMs), and broadband fluctuations which have been identified with low frequency zonal flows. Thus the primary goal of the present work was to search for the presence of such GAMs or zonal flows in the C-Mod, where they have not been seen previously. The present GPI measurements are localized near the outer midplane, so the local, and not the global, structure of the zonal flows can be directly measured.

A second motivation for the present work was to learn more about the radial velocity of the edge turbulence, since this can directly affect the radial transport. The time-averaged or convective velocity of edge turbulence was previously measured in C-Mod using GPI data [27-31], but the time-dependent velocity fluctuations were not evaluated. Radial turbulence velocity fluctuations have been measured locally with probes in many tokamaks [1-3], e.g. in DIII-D [32] and JET [33], but the poloidally-averaged radial velocities have not been measured. Thus the secondary goal of this paper is to evaluate the poloidally-averaged radial velocity fluctuations from the GPI data and compare them with the poloidal-averaged velocity fluctuations, and with the time-averaged or convective radial velocities determined from the same data.

The organization of this paper is as follows: the GPI diagnostic and data analysis technique is described in Sec. 2, the parameters of Alcator C-Mod and the database of shots used here is described in Sec. 3, and the results of this

analysis are described in Sec. 4. A summary and discussion of the results, including comparisons with previous experiments and theory, is given in Sec. 5, along with conclusions and suggestions for further work.

2. Diagnostic description and data analysis

This section describes the GPI diagnostic and data analysis: Sec. 2.1 describes the GPI diagnostic techniques, Sec. 2.2 describes the data processing and backgrounds, Sec. 2.3 discusses the interpretation of GPI signals, and Sec. 2.4 describes the data analysis methods used in the present paper. The C-Mod plasmas and database are described in Sec. 3, the analysis results are described in Sec. 4 and the discussion is in Sec. 5.

2.1 Gas puff imaging diagnostic

The gas puff imaging (GPI) technique has been described previously [27-31] so only an a brief description emphasizing the new features will be given here. The GPI diagnostic uses the neutral atom D_α (656.3 nm) or HeI (587.6 nm) line emission to measure the structure and motion of the edge turbulence in the plane perpendicular to the local magnetic field B, as illustrated in Fig. 1. The diagnostic region used in the present experiment covers a ~ 5.5 cm radial by ~ 5.5 cm poloidal region near the outer midplane separatrix (red box), which is viewed along the local B (~11° with respect to the toroidal direction. The gas cloud is used to spatially localize the D_α or HeI line emission along this sightline, so that the local turbulence structures perpendicular to B can be well resolved.

The D_2 or He gas puff is introduced by a set of four mm-sized holes in a manifold just behind the limiter shadow near the region to be imaged. The GPI gas cloud is viewed by a telescope mounted on the outer wall ~50 cm away along B, and the resulting image is transferred through a vacuum window to a custom-made 5 meter long 57x57 quartz fiber imaging bundle. Prior experiments used glass fiber optic bundles which were replaced in 2009 due to radiation darkening, most likely due to the high x-ray flux associated with lower hybrid current drive. The strength of the D_2 GPI puff is adjusted to give a D_α signal level at least 5 times larger than the D_α background level just before the GPI puff. For the cases with a He GPI puff into deuterium plasmas, the signal level of HeI with the puff is 10-30 times higher than the background level before the GPI puff.

The image at the other end of the fiber bundle is passed through a D_α or HeI filter, and viewed by a new Phantom 710 camera from Vision Research, Inc. For all experiments described in this paper the camera was operated at 391,000 frames/sec with an exposure time of 2.2 μs/frame. This is faster than previous cameras used on C-Mod, which was operated at 250,000 frames/sec [27-31]. The images for the present paper were digitized at 64x64 pixels/frame with a 12 bit dynamic range for at least 30,000 frames/shot (i.e. 75 msec/shot) just before and during the GPI gas puff.

The spatial resolution of the optical system is ~2-3 mm at the gas cloud, which is smaller than the typical turbulence size scale of ~0.5-1 cm. The spatial resolution of the turbulence also depends on the extent of the localization of the 3-D turbulence filament by the gas cloud, which in turn depends on the signal/background ratio, as described in the following section. The time between

frames is 2.5 μs, which is short enough to capture the most of the fluctuation spectrum. There was also a separate fast diode array which viewed the same gas cloud at a 0º with respect to the toroidal direction [30] with a higher bandwidth but a lower spatial resolution. Data from that diode array is not used in the present paper.

2.2 Data processing and backgrounds

The data for the present experiment were typically analyzed for a 20 msec long period near the peak of the GPI puff when the gas puffing rate and GPI signal level were approximately constant. The raw camera images for each frame were first normalized to a single 20 msec-averaged frame for that shot, in order to eliminate systematic pixel-to-pixel spatial variations due to the fiber bundle and optics. The resulting images show a smoothly varying space-time structure which clearly resolves the structure and motion of the turbulence, at least on a spatial scale ~0.5-5 cm. These images can be seen in sample videos [34].

For the GPI measurements made using D_α in this paper, the main background is due to wall recycling of deuterium outside the GPI puff but within the GPI field of view. Since these background neutrals are roughly uniformly distributed toroidally, the background contains the full the 3-D structure of the edge turbulence filaments within the GPI field of view (see Fig. 1). Thus this background consists of radially elongated 'hoop' structures connected to each bright turbulence structure. Since this background is also fluctuating, it can not easily be subtracted out. The effect of this background was minimized by increasing the D_2 GPI puff strength until the signal/background was ~5 or more

near the separatrix. This was high enough so that the local 2-D structure of the turbulence in the SOL could be clearly resolved up to 1-2 cm inside the region local separatrix. Farther inside this radius the D_α signal level due to the GPI puff decreases rapidly, so that the radial structure and motion of the turbulence can not be clearly resolved. This 3-D background effect is negligible when the GPI puff gas is He and the HeI line is used.

2.3 Interpretation of GPI signals

The interpretation of GPI signals has been discussed previously based on DEGAS 2 modeling of the neutral gas puff and atomic physics of D_α [35] and HeI [36]. The light emission in these lines is proportional to $n_o f(n_e,T_e)$, where n_o is the local neutral density and typically $f \sim n_e^{\alpha} T_e^{\beta}$, where typically $\alpha, \beta \sim 0.5\text{-}1.0$ near the peak of the GPI signal in C-Mod. Good agreement was obtained between the calculated and measured radial location of the time-averaged light emission from these lines, given the measured density and temperature profiles in C-Mod [35] and NSTX [36]. Atomic physics calculations indicated the response time of these lines to changes in n_e or T_e should be $\leq 1\ \mu$sec.

Thus the local fluctuations in GPI light emission are nonlinear functions of the local density and temperature fluctuations, assuming that the neutral density from the gas puff does not vary on the timescale of the turbulence. It was shown previously that this nonlinearity does not significantly affect the cross-correlation properties of the turbulence [37], i.e. the correlation lengths and correlation times are largely independent of α, β. These nonlinearities act like the contrast control of a TV monitor, in that they change the relative brightness

but not the structure or motion of objects. However, the relative GPI fluctuation level does retain a sensitivity to these nonlinearities, and so is not necessarily the same as the relative density fluctuation level. The interpretation of GPI signals does assume a correlation between the local electron density and temperature, since if these were uncorrelated the resulting line emission would be a mixture of the two time dependences. However, theoretical simulations of the C-Mod SOL plasma have shown a high correlation between n_e and T_e [38], as expected for ExB advection.

The interpretation of the 2-D GPI image sequences in terms of 2-D turbulence velocities has been discussed previously for both time-averaged analyses in C-Mod [27-31] and time-dependent analyses in NSTX [17,18]. The time-delayed cross-correlation analysis used in the present paper (Sec. 2.4) works best when these complicated structures move less than their scale size within a frame-to-frame time, i.e. for the present case when their velocity is $V \leq 0.8$ cm/2.5 μs ~ 3 km/sec. The natural unit for this velocity analysis is 1 pixel/frame or V~ 0.34 km/sec for the present cases, but averaging over many pixels or frames can resolve velocities significantly lower than this.

There are some additional limitations on the interpretation of the present 2-D GPI image sequences in terms of 2-D velocities vs. time. For example, motion along a direction in which there is no signal gradient can not be detected at all, and the cross-correlation technique used here tends to weight the most intense structures and to miss the weaker or smaller-scale ones. These limitations are discussed for GPI data analysis in [39] and for the similar time delay estimation method for BES data in [40]. There are also a fundamental limitations in interpreting the turbulence velocity in terms of local fluid velocity, as

discussed in Sec. 5.2.

2.4 Velocity analysis using 2-D cross-correlations

The turbulence velocity was estimated for these experiments using a time-resolved 2-D cross-correlation analysis code similar to the one used previously used to evaluate poloidal flows in GPI data from NSTX [17]. This technique is also similar to the time delay estimation method previously used to evaluate zonal flows from turbulence data in DIII-D [9.14]. The present analysis aims to search for zonal flows in the GPI data; thus, the once the local velocities are found, they are averaged over the poloidal field of view to evaluate (as well as possible) the large-scale zonal flow component of these velocities.

The first step in the analysis is to normalize each 64x64 frame from the GPI camera to the time-averaged frame, as described in Sec. 2.2. Two examples of such frames are is shown in Fig. 2, where the separatrix is shown by a dashed line, the limiter shadow by a dotted line, and the 5.5 cm x 5.5 cm frame was oriented so that radially outward is to the right, and the poloidal ion diamagnetic and grad-B directions are downward. The next step is to choose a single pixel within the analysis region defined by the black box in Fig. 2 (pixels 20-50 horizontally and 8-55 vertically). Then for this pixel for this frame, a short time series is created consisting of the normalized intensities at that pixel for a time period ±5 frames around the initial frame, i.e. a time series is formed with a length of 10 frames x 2.5 μs = 25 μs. Then a cross-correlation of this time series is done with a second time series (of the same duration) for each neighboring pixel, but centered on the *following* time frame. Then the *spatial location* of the maximum cross-correlation coefficient between the initial pixel's time series with

the time series in the next frame is found. This locates the place where the fluctuations in the initial pixel are most likely to be found in following frame, i.e. this finds the local motion of the turbulence between these two frames.

The spatial location of this maximum cross-correlation coefficient is then evaluated for each pixel in every frame. The radial and poloidal velocity for each pixel are then found from the horizontal and vertical displacements between the initial pixel and the pixel with the maximum cross-correlation in the next frame, using the calibration 1 pixel/frame =0.34 km/sec. This analysis requires correlating ~30x47 pixels over 16x16 neighboring points for each time step, i.e. ~2 billion correlations for a typical 20 msec analysis.

Finally, the poloidal and radial velocities for each pixel for each frame are poloidally averaged over each ~4 cm poloidal high column in the analysis region of Fig. 2 in order to evaluate the zonal flows in this region. This process is only an approximation to the ideal m=0 poloidal structure of these flows, but it is the best that can be done with the limited poloidal range of this diagnostic (see Sec. 5.2).

The search for the maximum cross-correlation is limited to ±8 pixels vertically (in the poloidal direction), which corresponds to a maximum detectable poloidal velocity of 8 pixels/frame ~2.7 km/sec in either direction. This was a compromise between having a reasonably large 4 cm poloidal averaging region, and having a reasonably large range of detectable velocities. The radial search range was bounded by the limiter shadow at the outside, and by the diminishing GPI signal on the inside. The resulting poloidally-averaged poloidal and radial velocities were almost always ≤1 km/sec, although individual pixels were

sometimes at the limit of this poloidal velocity range. A typical maximum cross-correlation coefficient using this velocity analysis procedure was 0.8, i.e. the turbulence structure largely moved as a 'frozen flow' over the 2.5 μs time delay between frames.

An example of the this analysis technique for the poloidal velocity is shown at the top left of Fig. 3. In this case the V_{pol} estimated for one column of pixels (at ρ =0.64 cm) and for one time (0.752561 sec) is plotted as a function of the poloidal position (i.e. vertical pixel) over a range of about ±2 cm in the analysis box of Fig. 2. The typical V_{pol} is in the range ±1 km/sec, although there is a significant variation of V_{pol} with vertical position, which is not surprising due to the intrinsically turbulent nature of the flow. For the rest of the analysis in this paper, *only the poloidal average of the poloidal velocity over the analysis box* of Fig. 2 will be used, which is illustrated for this case by the dashed line at the top left of Fig. 3. This is used to evaluate the zonal flow in this region. Some discussion of this limitations of this analysis is in Sec. 5.2.

The radial profile of the poloidally-averaged V_{pol} for this same time frame is shown by the solid line at the upper right of Fig. 3, and the 20 msec time-averaged profile of this poloidally-averaged radial profile of V_{pol} is shown by the dashed line. There is a significant radial variation of V_{pol} over the radial range -1 cm $\leq$ ρ $\leq$ 2 cm, which is the radial range of the analysis box for this case. Typical time dependences of the poloidally-averaged V_{pol} and V_{rad} are shown for a 1.2 msec (500 frame) interval at the bottom left of Fig. 3. The time-averaged radial velocity at this radius (ρ =0.32 cm) is V_{rad} ~ 0.5 km/sec (radially outward), while the time-averaged poloidal velocity is V_{pol} ~ -1 km/sec (in the ion

diamagnetic direction). The time-average of these time-dependent velocities agreed well with the time-average velocity obtained using cross-correlations made over a long (~ 10 msec) time series, as done previously data [29].

This time-dependent velocity analysis was checked by taking a typical frame of data and artificially oscillating it vertically and horizontally in a square-wave motion with various speeds and periods as a function time. The relative frequency response to this motion was ~30 kHz (to 1/e), which was set by the 25 μs length of the time series used in the cross-correlation analysis, as shown at the bottom right of Fig. 3. Frequency spectra of fluctuations in these velocities will be discussed in Sec. 4.

3. Database and edge turbulence characteristics

This section describes the C-Mod database used for this experiment, and summarizes the edge turbulence characteristics for this database. Since these edge turbulence characteristics are similar to those described previously for GPI measurements in C-Mod [27-31], they will not be discussed in detail. The turbulence velocity analysis is in Sec. 4.

3.1 Database for this analysis

The data used for this paper were all taken during the C-Mod 2009-2011 run periods using the midplane GPI camera running at 391,000 frames/sec. The GPI field of view remained constant with respect to the vessel during this period, although the separatrix location varied from shot-to-shot within this field of view.

All discharges were standard lower single-null diverted deuterium plasmas with a nominal size of R_o=0.67 m and a=0.23 m.

The list of the 30 discharges used in this paper is shown in Table 1. All GPI data for these 30 shots was taken during the steady-state portion of normal C-Mod discharges (the 31st shot was just before an L-H transition). These shots were selected to have q_{95}=3.4±0.4 in order for the local B field to be within ±2° of the GPI sightline angle to optimally resolve the 2-D turbulence structure. The range of plasma parameters was I=0.75-1.1 MA, B=3.6-6.1 T, line-averaged density <n> ~ 0.6-1.9 x10^{20} m^{-3} (i.e. n_G ~ 0.1-0.35), and stored energy W=21-76 kJ. Most discharges were Ohmic, but a few shots had up to ~2 MW ICRF. The outer midplane separatrix location varied from ~0.5-2.0 cm inside the outer limiter shadow location (0.905 m), and the GPI gas puff and optical filter were either D (656.3 nm) or He (587.6 nm). A measure of the poloidal velocity correlation related to the zonal flow is shown in the right column (see Sec. 4.4).

All 30 of these discharges were in L-mode, but one shot (#31 Table I) had an L-H transition shortly after the time of analysis. This case (1110114032) is discussed separately in Sec. 4.7. These 30 discharges covered six run days of GPI operation, with 17 shots done using the D_2 GPI puff and D_α filter, and 13 shots done using the He GPI puff and HeI filter. The only significant difference between the results for these two GPI gases was the lower background level for the He GPI cases; otherwise, the turbulence characteristics are essentially the same for either GPI gas for similar discharges.

3.2 Edge turbulence characteristics

As mentioned above, the general characteristics of edge and scrape-off-layer turbulence in this database are similar to those described previously for C-Mod [27-31]. Therefore in this section we just give a few examples of these characteristics in order to put the velocity analyses of Sec. 4 into context. All analyses in this sub-section are averaged over the 4 cm poloidal (i.e. vertical) range of interest as shown by the box in Fig. 2, and over a 20 msec time interval (~7800 frames).

Figure 4 shows the radial and poloidal correlation lengths evaluated for the top 30 shots in Table 1 at a radial location ρ~0.5 cm outside the separatrix. These correlation lengths were first evaluated locally for each point (assuming a Gaussian cross-correction fall-off), and then averaged over the poloidal analysis region shown in Fig. 2. These radial and poloidal correlation lengths are almost all within the range $L_{rad} \sim L_{pol} \sim 0.8 \pm 0.3$ cm (FWHM). Thus there are about 5 poloidal correlations lengths over the 4 cm poloidal analysis region of Fig. 2. There was no systematic difference in correlation lengths measured with D or He GPI in this database (the four shots with a somewhat higher radial correlation lengths of $L_{rad} \sim 1.2$ cm were in D, i.e. 1100721010-014). There was no strong dependence of these correlation lengths on the plasma current (at q_{95}=3.4±0.4), as was also the case in [29], or on the stored energy or line averaged density. However, there is a significant change in the turbulence near the density limit [31], which was not within this database.

Figure 5 shows the radial profiles of some edge turbulence quantities for the four typical shots highlighted in Table 1. At the top left are the radial profiles

of the relative GPI signal intensity, showing a peak within about ±0.5 cm of the separatrix (the separatrix was determined by EFIT and is uncertain by ~0.3 cm). The relative GPI fluctuation levels δI/I (RMS/mean) are shown for these same shots at the bottom left, and generally increase monotonically from δI/I ~ 0.05-0.2 at ρ~ -1.0 cm (inside the separatrix) to δI/I ~ 0.2-0.6 at ρ ~1.0 cm (outside the separatrix), as usual for tokamak edge plasmas. Also shown in Fig. 5 for these four shots are radial profiles of the radial and poloidal correlation lengths L_{rad} and L_{pol}, which are in the range L~0.5-1.0 cm (FWHM) in almost all cases. At the top right are the profiles of the autocorrelation time, which are in the range are τ~3-40 μs (FWHM), and at the bottom right are the maximum values of the cross-correlation coefficients used for the velocity analysis, which were all ~0.8.

3.3 Edge plasma characteristics

Edge Thomson scattering data was available for most of the shots of Table 1, and a summary of the typical edge electron densities and temperatures is shown in Table 2. Each number in this table is averaged over 3-4 similar shots and over a radial range of ±0.3 cm around the chosen radii of ρ = 0 and ±0.5 cm, with error bars from the variation in n_e and T_e over this radial range for these shots. Near ρ = 0, the average temperatures were T_e ~ 45 eV for the Ohmic shots and ~130 eV for the ICRH heated shot, and n_e ~ 3.5-9.5 x 10^{13} cm^{-3}. Although this table is written in terms of the distance from the separatrix, it should be noted that the separatrix location is uncertain to about 0.3 cm in C-Mod.

4. Evaluation of turbulence velocities

This section describes the evaluation of poloidally-averaged turbulence velocities derived from the analysis methods of Sec. 2 as applied to the GPI database of Sec. 3. Section 4.1 describes the time-averaged radial and poloidal velocities, Section 4.2 describes the probability distribution of these velocities, Section 4.3 describes the frequency spectra of these velocities derived from the time-dependent analysis, and Section 4.4 describes the radial profile of these frequency spectra. Then Section 4.5 describes the cross-correlations among radial and poloidal velocities and GPI signal level fluctuations, Sec. 4.6 compares the poloidal velocity spectra with magnetic fluctuation spectra, and finally Sec. 4.7 describes some results on the velocity analysis during transient events such as an L-H transition. Thus Sections 4.1 describes the time-averaged "mean flows" and Secs. 4.3-4.7 describe the characterization of time-dependent "zonal flows" in these plasmas.

4.1 Time-averaged turbulence velocities

Before discussing the time-dependent results derived from the cross-correlation analysis method of Sec. 2.4, we first present an overview of the time-averaged radial and poloidal velocities found by averaging the time-dependent analyses over a 20 msec analysis window. These results will be compared with the time-averaged velocities found in C-Mod using other methods in Sec. 5.3.

The top part of Figure 6 shows the radial profiles of the time-averaged poloidal and radial turbulence velocities as a function of radius for the same four shots of Fig. 5. The time-averaged poloidal velocity is typically $<V_{pol}(t)> \leq 1$

km/sec in the negative (ion diamagnetic and grad-B drift) direction, but the magnitudes and profile shapes of V_{pol} vary significantly from shot-to-shot. The time-averaged radial velocity is typically outward at for $\rho \geq -0.5$ cm at $\langle V_{rad}(t)\rangle \sim$ 0.2 km/sec, but slightly inward farther into the plasma. The middle of Fig. 6 shows the RMS fluctuation levels of these velocities, to be discussed in Sec. 4.2.

The bottom of Figure 6 shows the radial profiles of the time-averaged poloidal velocity for all 30 shots in the database. The error bars on the points in Fig. 6 are the RMS variations of these velocities over the averaging time interval of 20 msec. The average poloidal velocity is always in the ion diamagnetic drift direction, but there is a considerable shot-to-shot variation, as illustrated at the top of Fig. 6. The time-averaged radial velocity always outward in the SOL but inward (although small) for $\rho < 1$ cm. The relationship of this radial velocity to radial transport depends on the correlation with density fluctuations, as discussed in Sec. 5.5.

Figure 7 shows the time-averaged average poloidal and radial velocities at ρ=0.5 cm in the SOL for the same database as for the correlation lengths in Fig. 4. The error bars on the points in Fig. 7 are the RMS variations of velocities over the averaging time interval of 20 msec. There is little or no dependence of these time-averaged velocities on the plasma current I_p, the line averaged density $\langle n\rangle$, or the plasma stored energy W, as was also the case for the turbulence quantities in Fig. 4.

4.2 Distribution of turbulence velocity

A general result of these analyses is that there is a significant fluctuation level in the time-dependent poloidally-averaged turbulence velocities within the GPI field of view. This was already seen in the sample velocity signals vs. time in Fig. 3, and in the RMS velocity fluctuations averaged in Fig. 6, which had a fluctuating component of ~0.3 m/sec, i.e. comparable to the time-averaged velocities. This was further illustrated in Fig. 7, which shows the velocities calculated at $\rho \sim 0.5$ cm for all shots in the database, including the RMS fluctuations as error bars on the average velocities. Furthermore, this figure shows that there were no strong trends in the RMS radial or poloidal velocities as a function of stored energy, plasma current, or line-averaged density in this database (at this location). In all cases the velocity fluctuations are comparable to the mean velocities.

Figure 8 shows an example of the probability distributions of the radial and poloidal velocities for three different radii ($\rho = 0$ cm and $\rho = \pm 0.8$ cm) for one case (1110114026), averaged over 20 msec. The velocity distributions are all quite broad with a roughly Gaussian distribution with an RMS in velocity typically $\delta V \sim 0.3$ km/sec. The bottom of Figure 8 shows the distributions of V_{pol} as a function of V_{rad} for the same shot, where each point corresponds to the velocities for one frame for this shot. There is a significant correlation between the V_{pol} and V_{rad} for the $\rho \sim 0.0$ cm and $\rho \sim -0.8$ cm cases. These cross-correlation between radial and poloidal velocities *fluctuations* will be discussed further in Sec. 4.5.

4.3 Frequency spectra of turbulence velocity

To look for organized zonal flows within these fluctuations in turbulence velocity, it is helpful to examine the frequency spectra of these velocity fluctuations. Figure 9 shows two examples of the frequency spectra of V_{rad} (left) and V_{pol}(right) as a function of time over 20 msec at ρ = -0.5 cm for shot 1100120025 (top) and 1110114026 (bottom). These time-resolved spectra are evaluated using an FFT averaged over 800 frames (~2 msec) at each time point, and the spectra are uncorrected for the frequency response of the velocity analysis, i.e. the sensitivity to velocity fluctuations in this plot falls by about 1/e at ~30 kHz (see the "25 μs" curve of Fig. 2).

The case at the top (110110025) shows no apparent coherent features in the spectrum of either V_{rad} or V_{pol} in the range ~1-30 kHz, although there are intermittent bursts of duration ~1 msec with varying frequency in the range ~1-20 kHz. Most of the shots in Table 1 have spectra which look qualitatively similar to those at the top of Fig. 9. However, the case at the bottom (1110114026) does show a clear coherent feature at ~6-7 kHz in the V_{pol} spectrum for ρ = -0.5 cm. This coherent feature in V_{pol} persists over at least 70 msec, and is also seen at other radii (see next section). There is little or no coherent feature in V_{rad} at this frequency.

Figure 10 shows the V_{pol} frequency spectra for the four typical shots used in Fig. 6 for three radial locations, ρ= -0.8 cm, ρ=0.0 cm, and ρ=0.8 cm. The top plots show the two shots in Fig. 9, and the bottom plots show the two other typical shots, all of which are averaged over 20 msec (note the varying

vertical scales). The coherent mode at ~6-7 kHz in shot 1110114026 of Fig. 9 can be seen at all three radii in Fig. 10, although with a lower amplitude at ρ=0.8 cm. The more broadband, intermittent frequency spectrum seen in shot 1100120025 of Fig. 9 also seems to have a residual time-averaged spectral structure at ρ=-0.0 cm in Fig. 10, with different, and lower amplitude, spectra at ρ=±0.8 cm. One of the other two typical shots shown at the bottom of Fig. 10 (1091216030) has a similar but smaller broadband intermittent structure, but the other shot (1100824017) seems to have no significant spectral features.

The magnitude of this coherent velocity oscillation for 1110114026 near ~6-7 kHz between ρ= - 0.8 cm and ρ= - 0.0 cm is ~0.2 km/sec, as determined from comparing the peak in this spectrum with a forced oscillation of the raw image data at this frequency. The full amplitude of the poloidal motion corresponding to this oscillation is ~ 1 cm. However, this poloidal motion can not easily be seen in the movies of this shot [34] since the turbulence correlation times (~10-30 μs) are much shorter than the period of this oscillation (~150 μs).

4.4 Radial profiles of poloidal velocity spectrum

Radial profiles of the poloidal velocity fluctuation spectrum are illustrated in Fig. 11 for the top two shots of Fig. 10, each for three different times. These spectra are again calculated over 800 frames centered at the times shown in each panel. For the case at the top (1100120025), the velocity fluctuations have a band-like spectra extending over radius in the region ρ = -0.5 cm to +0.5 cm; however, this structure changes slowly in time over 20 msec, which leads to the broad and intermittent spectra shown in Figs. 9 and 10. In the

lower case (1110114026), the velocity fluctuations have a dominant peak near ~6-7 kHz everywhere in the region ρ = -1.0 cm to +0.5 cm for all times, which corresponds to the peak in the spectrum of Fig. 10. Other shots look very similar to the coherent case with a dominant peak at ~6-7 kHz (e.g 1110114027 and 1110114032), but most shots have broadband intermittent spectra like 11001120025 (e.g. 1100120026, 1100120027, 1091216028, 1091216029, and 10912116030). Surprisingly, shot 1110114023 did not have a coherent mode, even though it was similar to 11004026.

In order to help clarify the radial extent of these poloidally-averaged poloidal velocity fluctuations, a 20 msec time-averaged normalized cross-correlation coefficient $<\delta V_{pol}(r-\Delta/2)\ \delta V_{pol}(r+\Delta/2)>$ was calculated for all radii within the analysis box of Fig. 2 for all shots in Table 1, where Δ=0.35 cm. The maximum of this correlation coefficient was then found for each shot, and this coefficient is plotted in Figure 12 as a function of the line-averaged density for that shot (these values are also shown at the right of Table 1). There is a surprisingly clear trend toward an increase in this radial correlation coefficient as <n> is decreased, as shown at the left. Interestingly, the highest poloidal velocity cross-correlation (~0.8) was for the shot in which an L-H transition occurred just after the time analyzed (1110114032). The two typical shots with largest spectral features in Fig. 10 (i.e. 1110114026 and 1100120025) were located in the group of points in Fig. 12 at the lowest density and highest correlation (~0.6), while the shot with the smallest spectral features in Fig. 10 (i.e. 1100824017) was located at the highest density and lowest correlation (~0.25). The other typical shot (1091216030) was somewhere in between in density and correlation level. There was no obvious trend of the magnitude of these radial cross-correlation

coefficients with plasma current or stored energy in this database.

The minor radius of this maximum cross-correlation coefficient is shown at the right of Fig. 12 for the same database. These radii are in fairly uniformly distributed in radius over -2 cm to 1 cm with respect to the separatrix. The radius of the maximum cross-correlation is within ~0.5 cm of the separatrix for the three shots with high correlation mentioned above, i.e. 1100120025, 1110114026, and 1110114032. Radial profiles of these correlations for these typical cases are shown in the next section.

Note that the dependence of the maximum radial cross-correlation coefficient of δV_{pol} with density shown in Fig. 12 does not imply that the magnitude of δV_{pol} varies this way with density. In fact it does not, as shown for the four typical cases in the middle of Fig. 6, and for the larger database for ρ=0.5 cm in Fig. 7.

4.5 Correlations of radial and poloidal velocity

The radial profiles of various cross-correlations of the fluctuations in the poloidally-averaged δV_{pol} and δV_{rad} with each other and with the fluctuations in the GPI signal level are shown in Fig. 13 for the four typical shots used in Figs. 6 and 10. The radial profiles of cross-correlation coefficients between δV_{pol} and δV_{pol} at a Δr=0.35 cm radial separation are shown at the upper left of Fig. 15 (the maxima of these were shown in Fig. 12). These cross-correlations are ≥0.5 over the radial range ±1 cm for shot 1110114026, which was the shot with the 6-7 kHz coherent feature. The following shot (1110114027) was similar, and the pre L-H

transition shot (1110114032) has an even higher cross-correlation of ≥ 0.75 over this same spatial range (not shown). Thus the radial structure of the velocity fluctuations extends over at least ±1 cm around the separatrix in these cases with a coherent feature. For the less coherent cases like 110120025 and 1091216030 the cross-correlation is highest near the separatrix, but falls off inside and/or outside this radius.

The cross-correlation between the poloidally-averaged δV_{pol} and δV_{rad} at zero time delay and zero radial separation is shown at the upper right of Fig. 15. There is a significant positive cross-correlation outside the separatrix for at least 3 of these 4 shots (and also for the L-H transition shot, not shown). There was also a significant negative correlation farther inside for two of these shots. These cross-correlations can be related to the Reynolds' stress, as discussed in Sec. 5.5.

The cross-correlations of the GPI signal intensity fluctuations δI (also averaged over the poloidal analysis region) with δV_{pol} or δV_{rad} are shown at the bottom of Fig. 13. There appears to be a significant negative correlation of δV_{pol} with δI just inside the separatrix for 1110114026, but otherwise there is only a low correlation (≤ 0.2) for all other δV_{pol} cases, and for all correlations of δV_{rad} with δI. The possible relationship between these correlations and turbulent transport is discussed in Sec. 5.5.

4.6 Correlation with magnetic fluctuations

Figure 14 shows the V_{pol} power spectra vs. frequency for $\rho = 0$ cm for two shots (1100120025 and 1110114026), averaged 20 msec, overlaid with the

MHD power spectrum of poloidal magnetic field fluctuations from an edge magnetic coil (BP1T_GHK) for the same shots. The peaks in the spectrum of V_{pol} for shot 1100120025 (right) do not coincide with those in the magnetic spectrum. However, for the coherent mode in the V_{pol} spectrum of 1110114026 at ~6-7 kHz does coincide with an MHD peak at this frequency. A similar frequency match occurred for the similar shot 1110114027, and also for the L-H transition case 1110114032, during which the frequency-resolved coherence coefficient between V_{pol} and the magnetic signals was ≥90% at ~6 kHz. However, an apparently similar shot 1110114023 had neither a coherent peak in V_{pol} nor an MHD peak near 6-7 kHz. Thus there is a correlation between the edge poloidal velocity and magnetic fluctuations for the cases with the coherent V_{pol} feature.

4.7 Transient events

For all data discussed so far the turbulence velocities have been analyzed during stationary plasmas. However, for shot 1110114032 there was an L-H transition shortly after the analysis time of 0.90-0.92 sec. Figure 15 shows the V_{pol} spectrum vs. time for this shot when there was an L-H transition at 0.923 sec, and subsequent ELMs at 0.931 sec, 0.938 sec, and 0.948 sec.

At the left of Fig. 15 is the spectrum of V_{pol} vs. time at ρ = - 0.4 cm, which shows a sudden decrease in the coherent feature at ~6 kHz at the time of the L-H transition. At the right of Fig. 15 is the time dependence of the amplitude of this coherent feature in V_{pol} integrated over 5-7 kHz for three different radii ρ = 0.0 cm, and ρ = ±0.4 cm. For each of these radii the V_{pol}

amplitude decreases by a factor of x5-10 within ~10 msec after the transition, and the amplitude of the MHD mode at this frequency also decreases similarly at this time (not shown). It is interesting that the slow variations in V_{pol} before the transition are also highly correlated among these channels, as will be discussed briefly in Sec. 5.6. The V_{rad} signals show no coherent oscillation and no significant changes at the L-H transition.

Transient changes in the turbulence velocities were also seen during the ELMs of Fig. 15. The GPI signal level increases for ~1 msec in the SOL at the ELM crashes, similarly to NSTX [41]. The V_{pol} has several large oscillations before and during the crash, and there is a transient increase in V_{rad} at the crash. All signals return to their pre ELM state about 1 msec after the crash. One other example of transient behavior of turbulence velocities was shown for shot 1110114026 in Fig. 9, which had a sawtooth crash at 0.0911-0.912 sec. In this case there was a slight increase in the coherent oscillation frequency of V_{pol} coincident with the sawtooth crash, with a return to the original frequency after ~ 3 msec.

5. Discussion

This section contains a summary of the experimental results in Sec. 5.1, a discussion of their uncertainties and limitations in Sec. 5.2, a comparison with other time-averaged velocity measurements on C-Mod in Sec. 5.3, a comparison with the theory of zonal flows in Sec. 5.4, a discussion of velocity cross-correlations in Sec. 5.5, a discussion of the relationship to other experimental results in Sec. 5.6, and a conclusion in Sec. 5.7.

5.1 Summary of experimental results

The new results of this paper concern time-dependent measurements of the poloidal and radial velocity of the edge turbulence in C-Mod, evaluated using a cross-correlation analysis method as described in Sec. 2.4 and illustrated in Figs. 2 and 3. These velocities were averaged over the poloidal range of the GPI diagnostic to search for large-scale flows. Limitations of this velocity algorithm are discussed in Sec. 5.2.

The edge turbulence characteristics for the database of Table 1 were described in Sec. 3.2 and shown in Figs. 4 and 5, and are consistent with those described previously for Alcator C-Mod [27-31]. Figure 4 shows that the poloidal and radial correlation lengths are almost independent of the plasma current (at fixed q_{95}), density, and stored energy. Figure 5 shows that the radial correlation lengths are fairly independent of minor radius for four typical shots, and that the relative GPI fluctuation levels consistently decrease from the SOL to inside the separatrix, as usual for edge turbulence.

The time-averaged radial and poloidal velocities were described in Sec. 4.1 and Figs. 6 and 7. There was a considerable variation in the poloidal velocity profile among these shots, but the average poloidal velocity was in the ion diamagnetic drift (and grad-B drift) direction within ±2 cm of the separatrix. The radial velocity was consistently outward in the SOL, but was slightly negative (i.e. inward) for $\rho \leq -1$ cm. Figure 7 showed that there was no systematic variation of these time-averaged velocities with plasma current, density, or stored energy.

Radial profiles of the RMS fluctuation levels in the poloidally-averaged poloidal and radial velocity were also shown in Fig. 6 for the four typical cases. These fluctuations were typically at a level of ~0.2-0.4 km/sec, which was comparable to the mean or time-averaged velocities. The distribution functions of velocity were typically broad, as illustrated in Fig. 8, and there was some correlation between radial and poloidal velocity, also in Fig. 8. In all cases both the radial and poloidal velocities had a significant fluctuating component.

The frequency spectra of the poloidal and radial velocity fluctuations for two shots was shown in Fig. 9. For one case (1100120025) there were only random-looking intermittent peaks in the poloidal velocity spectrum, while for the other case (1110114026) there was a nearly coherent oscillation in the poloidal flow at ~6-7 kHz, which looked (at least superficially) like a GAM, as discussed in Sec. 5.4. There was no clear coherent peak in the radial velocity spectra, so further analysis was done only for the poloidal velocity spectra. Examples of these spectra for the four typical shots were shown in Fig. 10 for three different radii, and radial profiles of these spectra and three times for two shots are shown in Fig. 11. The coherent feature at 6-7 kHz of 1110114026 extends over at least ±1 cm around the separatrix, while the more complex spectrum of 1100120025 was localized within about ±0.5 cm of the separatrix.

A measure of the radial correlation of the poloidal flow fluctuations was shown in Fig. 12, which plotted the maximum of the normalized cross-correlation $<\delta V_{pol}(r-\Delta/2)\ \delta V_{pol}(r+\Delta/2)>$, where Δ=0.35 cm. This correlation showed a rather clear dependence on the line-averaged density, with the highest cross-correlations at the lowest densities. This suggests that density is a significant variable in determining the poloidal flow fluctuations in this database, perhaps due to

collisional damping, as discussed in Sec. 5.4.

Radial profiles of the cross-correlations among poloidal and radial velocity fluctuations and the GPI signal level fluctuations were shown in Fig. 13 for the four typical cases. The zero-time delay cross-correlation of $<\delta V_{pol}(r)\ \delta V_{rad}(r)>$ was significant, and will be related to Reynolds' stress in Sec. 5.5. The zero-time delay cross-correlations between δV_{pol} and δI_{GPI} were significant in only one case, and those between δV_{rad} and δI_{GPI} were small in all cases, as discussed in Sec. 5.6.

The frequency spectra of δV_{pol} were compared with the magnetic fluctuation spectra in Fig. 14, and a coincidence between the coherent δV_{pol} oscillation at 6-7 kHz and a large peak in MHD spectrum was found. The coherent δV_{pol} decreased significantly at the L-H transition, as illustrated by another shot in Fig. 15, and there were also transient variations of δV_{pol} during ELMs and sawtooth crashes.

5.2 Limitations and uncertainties in experimental results

A fundamental limitation of these results is that the velocity measured in this analysis is that of the small-scale turbulence seen in the GPI images, and not the fluid (or ExB) velocity of the plasma itself. Thus we need to assume that the turbulence motion in these images is dominated by the local ExB flow in order to interpret the poloidal oscillations in velocity as a zonal flow or the radial velocity as a convective transport. Although the poloidal velocity of edge turbulence has been identified with the zonal flow in previous measurements, e.g. [9,12], there

could be an additional velocity of the turbulence within the plasma rest frame. For example, it is sometimes assumed (although not proven) that edge turbulence moves poloidally at the electron diamagnetic drift speed in the plasma rest frame [1,2]. For a typical case near the separatrix (1110114026) where T_e~150 eV and L_n~3 cm (see Table 2), the time-averaged diamagnetic velocity is V_{pol}~1 km/sec, which is comparable to the measured poloidal turbulence velocity. However, the fluctuations in the diamagnetic drift speed can not be evaluated here, since there is not enough information on time-dependent density and temperature profiles.

The other major limitation of these results is that the poloidal velocities were averaged locally over 4 cm in the poloidal direction (about 5 poloidal correlation lengths), so the derived velocities not were not the truly global (i.e. m=0) component of these flows. Although a similar limitation applied to the many previous measurements of zonal flow, e.g. [9-19], it would be useful to search for zonal flows using two measurements separated by much larger distance, e.g. [20-26]. Also left somewhat uncertain in this analysis is the sensitivity of the velocity results to the amplitude of the turbulence, which might effect, for example, affect the interpretation of the apparent drop in the near-coherent flow feature after the L-H transition in Fig. 15.

There are also specific limitations to the velocity algorithm described in Sec. 2.4. The cross-correlation analysis searches only an 8x8 pixel range to find the best frame-to-frame match, so only velocities ≤ 2.7 km/sec can be found with this method (see also Sec. 5.3). These analyses also make the approximation that the poloidal direction is vertical in these images, so averaged over the ~1-2 mm variation in ρ in a given column (see Fig. 2). This is comparable to the spatial resolution of the diagnostic and smaller than the radial correlation length of the

edge turbulence, so it is not a significant limitation.

5.3 Comparison with other turbulence velocity analyses in C-Mod

Other techniques have been used previously to evaluate the time-averaged poloidal and radial turbulence velocity in Alcator C-Mod. Radial vs. poloidal velocity fields were first evaluated with a cross-correlation algorithm in [27] using 2-D GPI data taken at 250,000 frames/sec and averaged over 300 frames (i.e. 1.2 msec). Poloidal velocities inside the separatrix were found to be dominantly ~0.3-1 km/sec in the poloidal direction, and radial velocities outside the separatrix were at ~0.5 km/sec, i.e. similar to those found here (Fig. 6). Radial velocities of spatiotemporal structures (i.e. blobs) were subsequently evaluated using time-delayed cross-correlations within GPI images and between GPI images and a moving Langmuir probe [28]. A broad distribution of radial and poloidal structure velocities was found for V_{pol} within the range ±1 km/sec and for V_{rad} in the range -0.5 km/sec to + 1 km/sec, but with an average V_{rad} ~ 0.5 km/sec outward, i.e. also similar the distributions shown here in Fig. 8.

The time-averaged radial turbulence speed from GPI camera data was recently studied using a cross-correlation analysis for an L-mode plasma current scan in [29]. Outward radial speeds in the range V_{rad}~0.2 km/sec in the SOL were found at 0.8-1.1 kA, and reversal of the radial speed to inward propagation was found near the separatrix, both similar to the results of Fig. 6. A significant spread in the velocity distribution of blob structures was seen again. Most recently, GPI turbulence velocities in C-Mod in different density regimes were analyzed using both cross-correlation and conditional sampling techniques [31]. In the density range at $n/n_G \leq 0.3$, as used in the present paper, the time-averaged

V_{pol} were within ±1 km/sec and the time-average V_{rad}~0.3-0.5 km/sec, similar to Fig. 6.

A direct comparison was made between the time-averaged velocities obtained from a blob-tracking algorithm similar to [29] with the time-averaged velocities obtained from the algorithm of Sec. 2.4 here. The results were very close to each other in magnitude and radial profile, i.e. differing by an average of only ~0.05 km/sec. A direct comparison was also made between the cross-correlation and the conditional averaging algorithms of [31] and the algorithm of Sec. 2.4. The conditional sampling velocities were close to those obtained here where they could be compared in the SOL, but in some cases the cross-correlation algorithm of [31] produced velocities which differed from those obtained here by up to ~0.5-1 km/sec. This is most likely due to a different type of space and time-averaging used in the two different algorithms. This points out that the turbulence velocities obtained for these GPI images do depend somewhat on the algorithm used to extract them.

Finally, a Fourier analysis of the wave-number vs. frequency spectrum of GPI data taken using the 2-D photodiode array [30] shows time-averaged poloidal phase velocities of ~2 km/sec in the ion diamagnetic drift, along with a ~4 km/sec phase velocity in the electron diamagnetic drift direction inside the separatrix. These poloidal phase velocities are significantly higher than the poloidal velocities determined from the cross-correlation analysis in the present paper. A detailed analysis of the difference between these two techniques is important, but deferred to a future publication.

5.4 Comparisons with theories of zonal flow

The main motivation for this study was to search for edge zonal flows in Alcator C-Mod, which have not been seen previously in this device. The result were that some evidence for zonal flows was found, although a clear quantitative connection between experiment and theory has not been established, as described below.

The clearest evidence for a zonal flow in this experiment comes from the cases with a coherent oscillation at 6-7 kHz in the poloidal velocity (e.g. shot 1110110026), as shown at the bottom right of Figs. 9. This oscillation, when it occurred, had a near-constant frequency over at least ±1 cm around the separatrix, as shown in Figs. 10, 11, and 13, and was correlated with magnetic fluctuations at the same frequency, as shown in Fig. 14. All of the shots with this coherent feature had ICRF heating, although shots with somewhat lower ICRF power had no such an oscillation (e.g. 1100824014, 1100824015).

Somewhat less clear, but still interesting, are the cases with a broadband intermittent spectrum in the poloidal velocity (e.g. shot 1100120025), as shown at the top right of Fig. 9. These cases had a complex spectrum in the range ~1-20 kHz, which varied with time but which was correlated over about ±0.5 cm near the separatrix, as shown in Figs. 10, 11 and 13, which is comparable to the radial scale length of the turbulence. The radial correlation of these complex poloidal flows had a clear dependence on the line-averaged density, as shown in Fig. 12. However, at the highest densities (e.g. shot 1100824017) it was not clear whether the small poloidal fluctuations detected by this analysis were large-scale zonal flows, or instead the residual result of averaging over random small-scale flows

due to turbulence.

The most likely theoretical candidate to explain the coherent oscillations in this experiment is a geodesic acoustic mode (GAM), such as seen in many previous experiments (see Sec. 5.6). An approximate formula for the expected frequency of a geodesic acoustic mode (GAM) for a shaped tokamak with aspect ratio A, elongation κ, and edge safety factor q is [42]: $f=G\ c_s/(\pi R)$, where the geometrical factor is $G = 2^{-0.5}\ (2/(1+\kappa))\ (1+1/(2\ A^{2/3}))\ (1+1/(4q^2))$ and $c_s = [\gamma Z(T_e+T_i)/M_i]^{0.5}$. For C-Mod: κ=1.6, A=3, q=3.4, Z=1, M_i=2, and assuming the for the shot with a coherent peak in V_{pol} for ρ=0 cm (1110114026) $T_i=T_e$=150 eV and γ=4/3, this frequency is f_{GAM}~34 kHz. However, there is quite a large variation in T_e (and presumably T_i) over the radial range in which the oscillation is observed; for example, T_e=36-340 eV for this shot over $\rho = \pm 0.5$ cm (see Table 2), which implies a radial frequency variation of f~17-52 kHz which is not observed in the experiment. Thus the identification of this mode with a GAM is inconclusive until the radial structure of this mode us understood.

The broadband and intermittent poloidal velocity fluctuations seen in this experiment might be related to the 'zero mean frequency' zonal flows described by other theoretical models [4]. These flows can have a radial scale length comparable to the turbulence and do not have a single frequency. They can in theory be affected by collisional damping in the edge, which might explain the increased radial correlation as the line-averaged density decreased (Fig. 12). Collisional damping is approximated as [4]: $\gamma = \omega_t^2/\nu_{ii}$, where $\omega_t = v_i/qR$ and ν_{ii} is the ion-ion collision frequency. For typical edge parameters for 1100120025 of T_i ~ 50 eV and n ~ 4×10^{13} cm^{-3}, this give γ ~ 5000 sec^{-1}, which is not inconsistent

with the duration of the bursts of flow seen for this shot at the top of Fig. 9. This dependence might explain at least qualitatively the density dependence shown in Fig. 12, although the boundary between broadband intermittent zonal-type flows and random turbulence at high density in Fig. 12 is not yet clear.

The coincidence between the coherent poloidal velocity oscillations and magnetic field fluctuations shown in Fig. 14 is not yet explained. Possible candidates include a magnetic component of the usual electrostatic GAMs [43], and an energetic particle-driven GAM [44-46], or a zonal magnetic field [47]. A few similar observations have been made previously, as discussed in Sec. 5.6.

In conclusion, there is not yet a clear connection between the poloidal flow fluctuations seen in this experiment and the theory of zonal flows or GAMs. Such a comparison would benefit from a specific simulation of zonal flows in these C-Mod edge plasmas in L-mode, which has not yet been done. However, a simulation edge turbulence in C-Mod H-mode plasmas is in progress [48].

5.5 Velocity cross-correlations

The zero-time cross-correlations of the poloidally-averaged V_{pol} and V_{rad} with each other and with the GPI signal fluctuations were shown for the four typical shots in Fig. 13. These correlations can in principle provide insight into flow generation and turbulent transport due to these fluctuations.

The normalized cross-correlation coefficients $<\delta V_{pol}\ \delta V_{rad}>$ at the upper right of Fig. 13 showed a significant positive correlation of ~0.3-0.5 just outside the separatrix for three of these four shots. This implies that there is a correlation

between outward radial velocity fluctuations and poloidal velocity fluctuations in the electron diamagnetic drift direction (both velocities as usual averaged over the poloidal extent of the GPI view). This correlation can be related to the Reynolds' stress, e.g. [49,50] $d/dr\langle\delta V_{pol}\ \delta V_{rad}\rangle = \nu_{damp}V_{pol}$, where ν_{damp} is the damping rate of the poloidal flows generated by this correlation. From Fig. 13, $d/dr\langle\delta V_{pol}\ \delta V_{rad}\rangle \sim 0.4/1$ cm near $\rho \sim 0.5$ cm where $V_{rad} \sim 0.2$ km/sec, which implies $\nu_{damp} \sim 0.4\ V_{rad}/1\ \text{cm} \sim 10^4\ \text{sec}^{-1}$. This is comparable to the zonal flow collisional damping rate of 5000 sec^{-1} estimated in Sec. 5.4, and also to a possible damping due to charge exchange of ions with neutrals, i.e. $\nu_{io} = n_o \langle\sigma v\rangle_{io} = (2\text{x}10^{-8}\ \text{cm}^3/\text{sec})(10^{12}\ \text{cm}^{-3}) \sim 2\text{x}10^4\ \text{sec}^{-1}$, assuming $n_o=10^{12}\ \text{cm}^{-3}$. Obviously the this estimate of the poloidal flow damping is highly uncertain at present.

The normalized zero-time cross-correlation coefficients $\langle\delta V_{pol}\delta I_{GPI}\rangle$ shown at the lower left of Fig. 13 are largest for the shot with the near-coherent oscillation in V_{pol} (1110114026). This suggests that there is a decrease in the turbulence level associated with a positive (i.e. electron diamagnetic drift) velocity fluctuation in this case. A similar correlation was seen in the 'quiet periods' in NSTX [17]. However, in other experiments a 90° phase shift was seen between the turbulence level and the zonal flow (i.e. poloidal velocity fluctuation), similar to a 'predator-prey' relationship. Further investigation of this phase relationship is important but beyond the scope of the present paper.

Finally, the zero-time cross-correlation coefficients $\langle\delta V_{rad}\ \delta I_{GPI}\rangle$ are shown at the lower left of Fig. 13. There was only a small (≤ 0.2) correlation between these quantities in all cases. However, even a small level of this correlation is sufficient to cause significant radial transport. For example, if this

correlation is taken to be 0.1, and a typical radial velocity fluctuation level is δV_{rad} ~0.2 km/sec (Fig. 8), and if the local $\delta n/n$ is assumed to be the same as the rGPI fluctuation level $\delta I_{GPI}/I$ of 10% near the separatrix (Fig. 5) where $n_{edge} \sim 5\times10^{13}$ cm^{-3}, then the local particle flux is $\Gamma = \langle\delta V_{rad}\ \delta n\rangle \sim (0.1)\ (0.1)\ n_{edge} V_{rad} \sim 10^{16}$ particles/cm^2-sec. Assuming a surface area for particle loss of $(2\pi R)(2\pi\kappa a) \sim 10^5$ cm^2, the resulting particle loss would be $\sim 10^{21}$ sec^{-1}, which is comparable to expected global loss rate of a C-Mod plasma with an average density of 10^{14} cm^{-3}, a volume of ~ 1 m^3, and a particle confinement time of 0.1 sec. Thus even the small cross-correlation levels of $\langle\delta V_{rad}\ \delta I_{GPI}\rangle$ in Fig. 13 may cause significant radial transport.

5.6 Relationship to results from other experiments

The main new results from this paper concern the time-dependent measurements of the poloidal velocity of turbulence motion in C-Mod in the frequency range ~1-30 kHz. These results are at least qualitatively similar to several results from other experiments. Note that spectroscopic measurements of plasmas velocity using diagnostics such as CHERS are (so far) too slow kHz to evaluate zonal flows in this frequency range.

Coherent fluctuations in edge poloidal velocity in the frequency range ~5-20 kHz have been measured in many tokamaks and identified as geodesic acoustic modes (GAMs). For example, the poloidal velocity of GAMs have been measured using Langmuir probes in T-10 [21], visible imaging in DIII-D [9], Doppler reflectometry in ASDEX Upgrade [12,15], and heavy ion beam probes in JFT-2M [11] and JIPPT-IIU [13]. The coherent fluctuations observed here in

Figs. 9-11 for shot 1110114026 is in this frequency range, and the poloidal velocity fluctuation level of ~0.2-0.6 km/sec seen here (Fig. 6) is similar poloidal velocity fluctuations seen in GAMs, e.g. ~0.2-0.8 km/sec in ASDEX [15]. However, the present results show these oscillation extend outside the separatrix, which was not seen in any previous results, and the frequency of GAMs in previous results generally increased toward the core, which was not seen here.

A coincidence between the coherent poloidal flow oscillations and edge magnetic fluctuations, such seen here in Fig. 14, was previously observed for GAMs in T-10 [22] and for energetic particle-driven MHD bursts in DIII-D [44] and CHS [46]. It is interesting to note that the coherent oscillation seen here occurred only during discharges with ICRH heating, which presumably had energetic ion tails. However, a direct connection between this mode and energetic ion loss has not been established.

The disappearance of the coherent V_{pol} oscillations at the L-H transition shown here in Fig. 15 is qualitatively similar to the behavior seen in NSTX [17], ASDEX Upgrade [19] and DIII-D [26] and TJ-II [7]. The very low frequency 'bursting' or 'quiet periods' seen previously in the V_{pol} and turbulence levels before the L-H transition in these devices may also be similar to the ~0.5 kHz oscillation in the V_{pol} oscillations before the L-H transition in Fig. 14.

Broadband fluctuations in edge poloidal velocity, i.e. 'zero-frequency' zonal flows, have also been measured in a similar frequency range in several tokamaks. For example, broadband low frequency zonal flows were seen with BES in the frequency range 1-10 kHz in the core of DIII-D [14], and broadband zonal flows were measured with probes in the frequency range 0.5-4 kHz in the

edge of HT-7 [10] and HL-2A [22]. Relatively little is known about such fluctuations, so is possible that the broadband V_{pol} spectra such as shown for shot 1100120025 in Figs. 9-11 are similar to these other experiments. The most interesting characteristic of these fluctuations in the present experiment is their decrease with increasing density shown in Fig. 12, which is qualitatively similar to the decrease in GAM amplitude seen in previous experiments, attributed to collisional damping [15].

There have been many previous measurements of edge and SOL radial velocity fluctuations using probes [1-3], which have been used to estimate the local turbulent particle transport $<\delta V_{rad}\ \delta n>$. For example, δV_{rad} distributions in the range ~1 km/sec were seen in DIII-D [32] and JET [33] which are at least qualitatively similar to the V_{rad} distributions shown here in Figs. 8. Note however that the V_{rad} calculated here were averaged over the poloidal viewing region of ~5 poloidal correlation lengths, while the previous measurements were more local.

5.7 Conclusions and further directions

This paper described an analysis of poloidal velocity fluctuations in the edge turbulence of Alcator C-Mod as measured by the GPI diagnostic near the outer midplane separatrix. These velocity fluctuations were either coherent at ~6-7 kHz or broadband in the range ~1-20 kHz, and had an amplitude comparable to the mean (i.e. time-averaged) poloidal velocity. We conclude that some of these results are at least partially similar to the GAMs and/or zonal flows described in theory and previous experiments, as discussed in detail in Secs. 5.4 and 5.6.

The most important diagnostic improvement would be to have GPI views at other poloidal and/or toroidal locations in order to check the large-scale n=0, m=0 nature of the zonal flow, as done previously with other zonal flow diagnostics. Further systematic experiments would be useful to clarify the location in parameter space of the coherent poloidal velocity oscillations, which were seen here only during low density, RF heated plasmas at 5.3 T and 1.0 MA. It would also be interesting to examine more L-H transitions to determine of these oscillating poloidal flows were somehow causing the transition.

Theory and/or simulations should be done specifically to evaluate zonal flows for plasma parameters of the C-Mod edge. These simulations could help guide further searches for zonal flows in C-Mod, including truly 'zero frequency' modes which are difficult to distinguish from mean flows. Given the observed correlation of the coherent flows with MHD activity, it would also be useful to calculate the magnetic component of such zonal flows, and also the poloidal flows associated with normal MHD activity, in order to clarify this relationship.

Acknowledgments: We thank for their contributions or comments: B. Davis, D. D'Ippolito, T. Golfonopolus, K. Hallatschek, T.S. Hahm, B. LaBombard, D. Russell, D. Stotler, G. Tynan and Alcator C-Mod Team. This work was supported in part by US DOE Contracts DE-AC02-09CH11466 and DE-FC02-99ER5412.

Table 1: Shot list

shot	time (sec)	Ip (MA)	B(T)	$\langle n_e \rangle$ 10^{20} m^{-3}	W (kJ)	P_{RF} (MW)	sep. (m)	GPI gas	VpVp corr.
1091216028	1.41	1.00	5.21	1.41	46.4	0	0.891	D	0.465
1091216029	1.41	0.99	5.21	1.16	40.5	0	0.892	D	0.467
1091216030	***1.41***	***0.99***	***5.20***	***1.13***	***38.4***	***0***	***0.893***	***D***	***0.436***
1100120006	0.76	1.02	5.42	1.13	42.6	0	0.886	D	0.435
1100120008	0.76	1.02	5.44	1.10	41.4	0	0.887	D	0.443
1100120025	***0.76***	***0.81***	***3.63***	***0.80***	***21.3***	***0***	***0.886***	***D***	***0.6***
1100120026	0.76	0.81	3.62	0.82	21.5	0	0.886	D	0.621
1100120027	0.76	0.81	3.63	0.79	22.4	0	0.887	D	0.6
1100721010	1.25	1.09	5.39	1.12	36.4	0	0.893	D	0.407
1100721011	1.25	1.09	5.38	1.22	48.1	0	0.895	D	0.397
1100721012	1.25	1.09	5.38	1.31	43.4	0	0.894	D	0.412
1100721014	1.25	1.09	5.39	1.15	37.0	0	0.895	D	0.438
1100803008	1.26	0.79	4.05	1.08	26.7	0	0.898	He	0.638
1100803015	1.26	0.78	4.05	1.62	28.4	0	0.899	He	0.414
1100803020	1.26	0.78	4.06	1.66	21.2	0	0.899	He	0.393
1100803022	1.26	1.03	5.39	1.60	35.7	0	0.900	He	0.332
1100824014	1.07	0.89	5.37	1.58	43.2	0.59	0.893	D	0.507
1100824015	1.07	0.90	5.37	1.59	46.6	0.77	0.893	D	0.547
1100824017	***1.07***	***1.08***	***5.37***	***1.76***	***57.2***	***0***	***0.893***	***He***	***0.234***
1100824019	1.07	1.08	5.37	1.90	51.0	0	0.894	He	0.212
1100824021	1.07	1.09	5.37	1.73	46.8	0	0.895	He	0.239
1100824023	1.07	1.08	5.37	1.74	44.8	0	0.895	He	0.418
1100824024	1.07	1.08	5.37	1.83	52.9	0	0.894	He	0.165
1100824025	1.07	1.08	5.37	1.84	49.3	0	0.893	He	0.16
1100824026	1.07	1.09	5.37	1.73	46.2	0	0.893	He	0.268
1100824028	1.07	1.09	6.12	1.65	39.2	0	0.895	He	0.302
1100824029	1.07	1.09	6.11	1.42	30.4	0	0.897	He	0.358
1110114023	0.91	1.00	5.26	0.76	76.3	1.88	0.895	D	0.569
1110114026	***0.91***	***1.00***	***5.26***	***0.67***	***60.3***	***1.63***	***0.895***	***D***	***0.602***
1110114027	0.91	1.00	5.26	0.71	58.3	1.78	0.896	D	0.609
1110114032	0.91	0.91	4.59	0.70	58.1	1.84	0.894	D	0.778

Table 2: Typical edge density and temperature

parameter	$n/10^{20}$ cm^{-3}	T_e (eV)	$n/10^{20}$ cm^{-3}	T_e (eV)	$n/10^{20}$ cm^{-3}	T_e (eV)
radius (cm)	-0.5 ±0.3	-0.5±0.3	0±0.3	0±0.3	0.5±0.3	0.5±0.3
1091216030	0.84 ± 0.15	90 ± 26	-	-	-	-
1100120025	0.42 ± 0.11	104 ± 54	0.35±0.08	45±23	0.44 ± 0.04	21 ± 10
1100824017	1.2 ± 0.1	84 ± 30	0.96±.22	46±16	0.94 ± 0.18	28 ± 11
1110114026	0.47 ± 0.10	340 ± 160	0.42±0.13	132+103	0.35 ± 0.13	36 ± 32

References:

[1] Wootton A J et al 1990 Phys. Fluids B 2 2879

[2] Zweben S J et al 2007 Plasma Phys. Control. Fusion 49 S1

[3] Boedo JA 2009 J. Nucl. Mat. 390-391 29

[4] Diamond PH et al 2005 Plasma Phys. Control. Fusion 47 R35

[5] Tynan GR, Fujisawa A, and McKee G 2009, Nucl. Fusion 51 131001

[6] Fujisawa A 2009 Nucl. Fusion 49 013001

[7] Hidalgo C 2011 Plasma Phys. Control. Fusion 53 074003

[8] Stroth U et al 2011 Plasma Phys. Control. Fusion 53 024006

[9] McKee GR et al 2003 Phys. Plasmas 10 1712

[10] Xu GS et al 2003 Phys. Rev. Lett. 91 125001

[11] Hamada Y Nucl. Fusion 2005 45 81

[12] Conway GD et al 2005 Plasma Phys. Control. Fusion 47 1165

[13] Ido T et al 2006 Plasma Phys. Control. Fusion 48 S41

[14] Gupta et al 2006 Phys. Rev. Lett. 97 125002

[15] Conway GD et al 2008 Plasma Phys. Control. Fusion 50, 085005

[16] Xu GS et al 2009 Nucl. Fusion 49 092202

[17] Zweben SJ et al 2010 Phys. Plasmas 17 102502

[18] Sechrest Y et al, 2011 Phys. Plasmas 18 012502

[19] Conway GD et al 2011 Phys. Rev. Lett. 106 065001

[20] Fujisawa A 2004 Phys. Rev. Lett. 93 165002

[21] Melnikov AV et al 2006 Plasma Phys. Control. Fusion 48 S87

[22] Liu AD et al 2009 Phys. Rev. Lett. 103, 095002

[23] Kramer-Flecken A et al 2009 Plasma Phys. Control. Fusion 51 015001

[24] Xu Y et al 2011 Nucl. Fusion 51 063020

[25] Silva C et al 2011 Nucl. Fusion 51 063025

[26] Schmitz L et al ?? Peebles DIII-D

[27] Terry J et al 2005 J. Nucl. Mat. 337-339 322
[28] Grulke O et al 2006 Phys. Plasmas 13 012306
[29] Zweben SJ et al 2010 J. Nucl. Mat.
[30] Czeigler I et al 2010 Phys. Plasmas 17 056129
[31] Agostini M et al 2011 Nucl. Fusion 51 053020
[32] Boedo JA et al 2001 Phys. Plasmas 8, 4826
[33] Goncalves et al 2005 J. Nucl. Mat 337-339 376
[34] see http://www.pppl.gov/~szweben/CMod2010/CMod2010.html
[35] Stotler DP et al 2003 J. Nucl. Mat 313-316 1066
[36] Stotler DP et al, 2007 J. Nucl. Mat. 363-365 686
[37] Zweben SJ et al 2004 Nucl. Fusion 44 134
[38] Zweben et al 2009 Phys. Plasmas 16 082505
[39] Munsat T and Zweben S 2006 Rev. Sci. Inst. 77 103501
[40] Holland C et al 2004 Rev. Sci. Inst. 75 4278
[41] Maqueda RJ et al 2009 Phys. Plasmas 16 056117
[42] Hager R or Hallatschek K best reference to GAM formula
[43] Hallatschek K and McKee G 2011 EPS meeting P.2132
[44] Nazikian R et al 2008 Phys. Rev. Lett. 101, 185001
[45] Fu GY 2008 Phys. Rev. Lett. 101 185002
[46] Ohshima S et al 2007 Plasma Phys. Control Fusion 49 1945
[47] Fujisawa A et al 2007 Phys. Rev. Lett. 98 165001
[48] Russell DA, 2011 private communication
[49] Tynan GR et al 2009 Plasma Phys. Control. Fusion 51 124055
[50] Windisch T et al 2011 Plasma Phys. Control. Fusion 53 085001

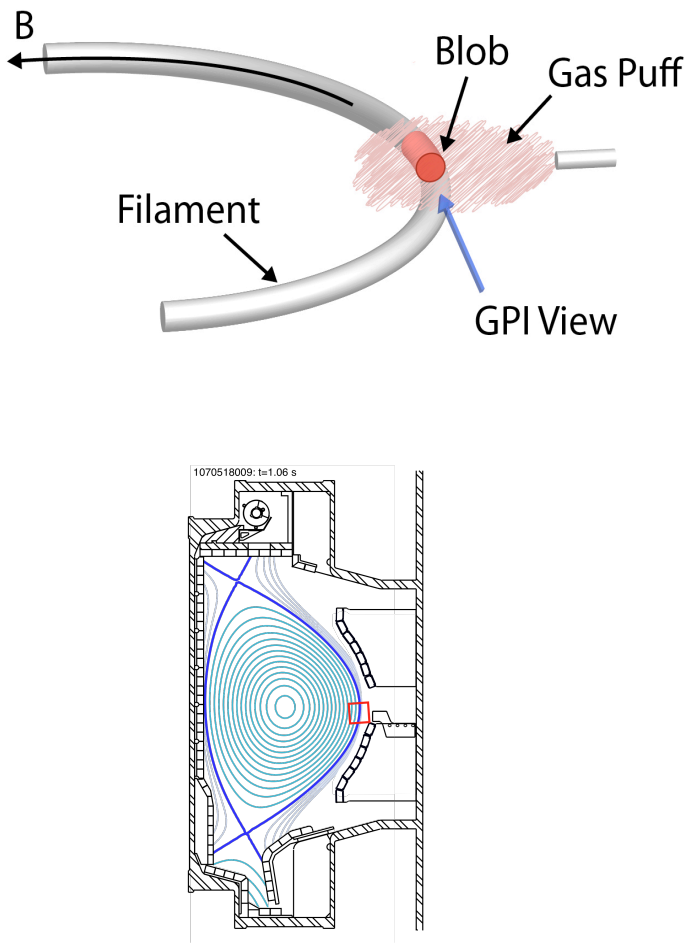

Fig. 1 – Schematic illustration of the GPI diagnostic geometry (top), and the location of the GPI camera field of view fn the present experiment (bottom, red box). The GPI diagnostic views the D_α or HeI light emitted by a neutral gas cloud along the local B field direction, in order to image the 3-D 3-D turbulence filament in the radial vs. poloidal plane across B.

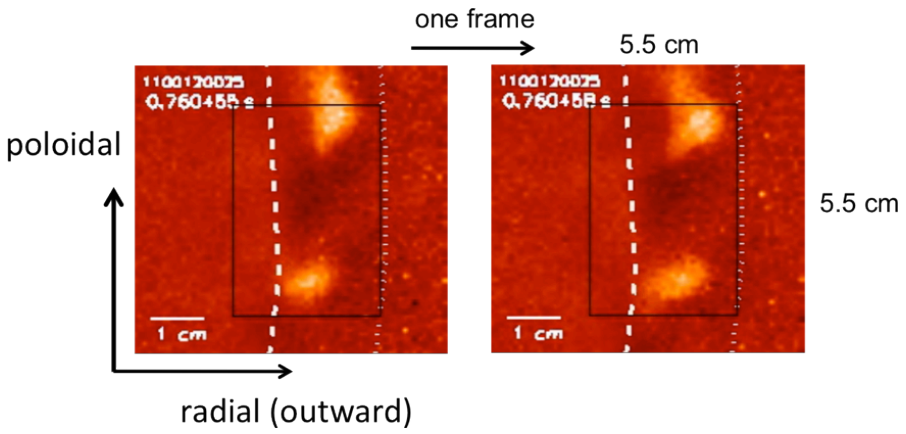

Fig. 2 – Example of two pair of successive normalized images separated by 2.5 μs, each with an exposure time of 2.2 μs. The signal level is shown in a false color scale, the separatrix is the dashed white line, the limiter (RF antenna) shadow is shown by the dotted white line, and the black box is the data analysis region.

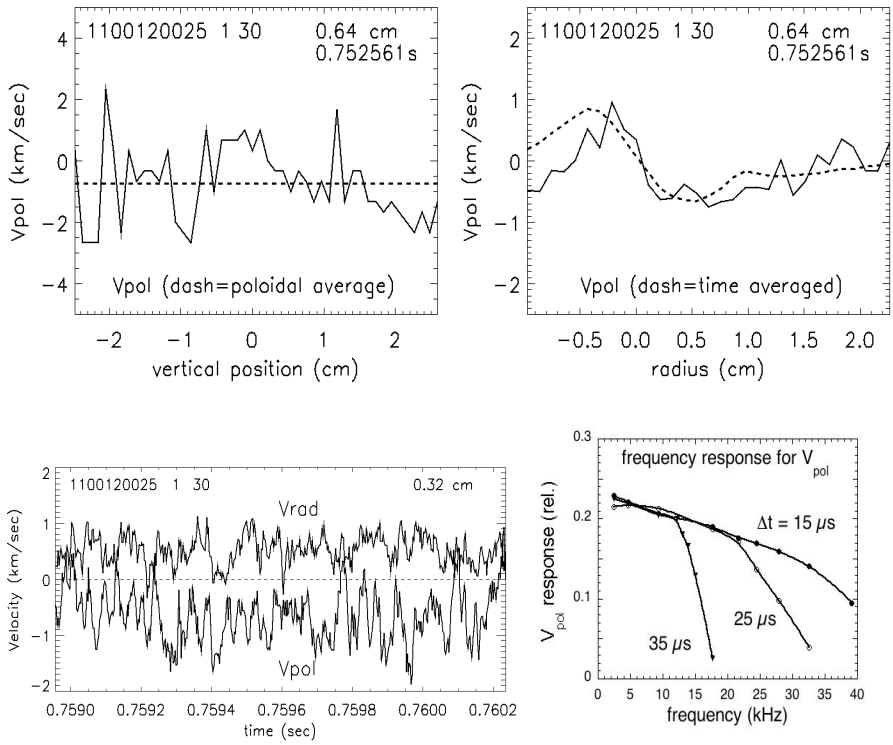

Fig. 3 – Example of a cross-correlation analysis for the poloidal velocity. At the upper left is the local V_{pol} vs. the vertical pixel (poloidal coordinate) for one radius for one frame. At the upper right is the radial profile of the poloidally-averaged V_{pol} for one frame, and also the 20 msec time-averaged V_{pol}. At the lower right are typical poloidally-averaged V_{pol} and V_{rad} vs. time for a single radius (i.e. horizontal pixel). At the lower right is the relative frequency response of this analysis to an artificial square-wave velocity imposed on this turbulence.

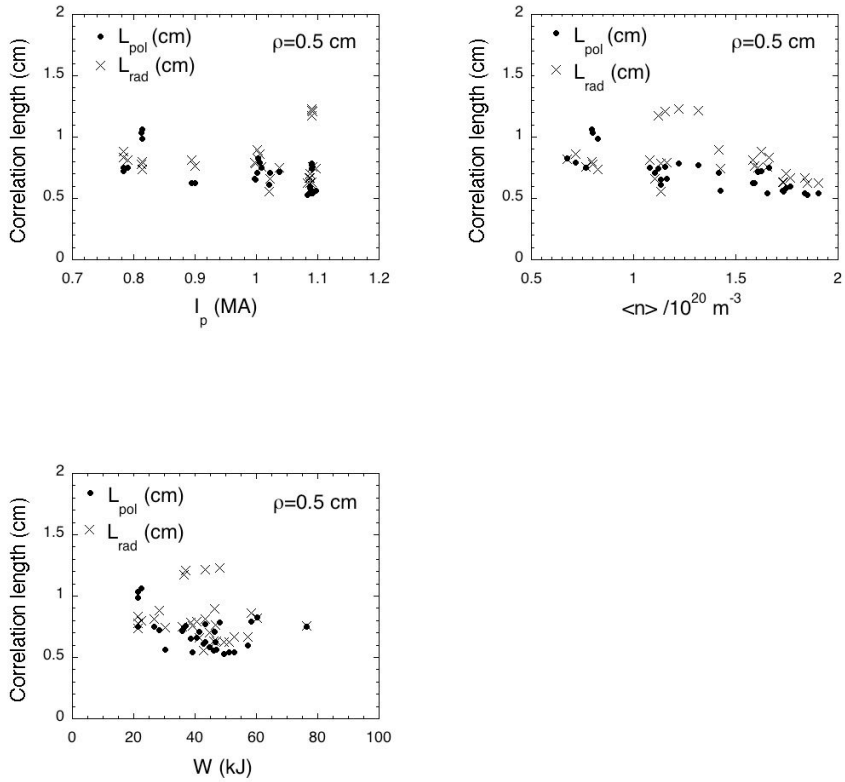

Fig. 4 – Radial and poloidal correlation lengths for the 30 shots in this database, all evaluated at ρ=0.5 cm outside the separatrix. There are only small variations in correlation length over the range of plasma current I_p, line-averaged density <n>, and plasma stored energy W in this database (all with $q_{95} \sim 3.4 \pm 0.4$).

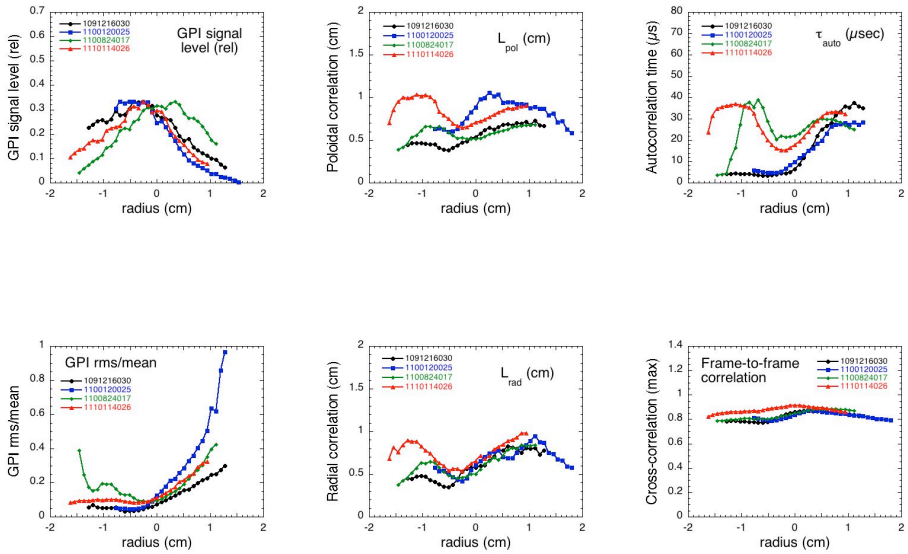

Fig. 5 – Typical radial profiles of turbulence characteristics for four typical shots in this database, averaged over the poloidal analysis region shown in Fig. 2. At the top left are the relative GPI signal profiles, at the bottom left are the relative GPI fluctuation levels, in the middle are the poloidal and radial correlation lengths, at the top right are the autocorrelation times, and at the bottom right are the maximum cross-correlation coefficients from the frame-to-frame velocity analysis.

ARD 8/9/11 8:52 AM
Comment:

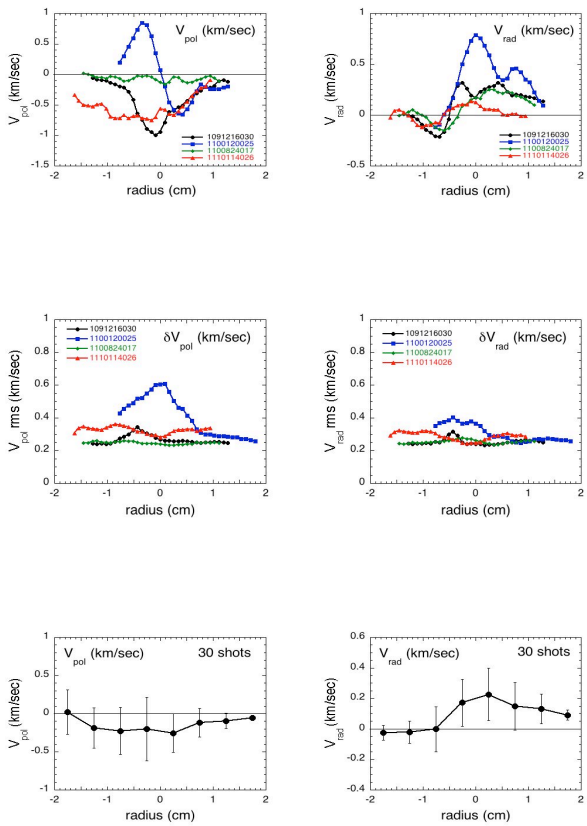

Fig. 6 - Radial profiles of the poloidally-averaged V_{pol} and V_{rad} for four typical shots (top), the RMS fluctuation levels in these velocities (middle), and average of these velocities for the 30 shot database (bottom). There is a fairly wide range of profile shapes for V_{pol} within this radial range, but on average the poloidal velocity is ~0.2 km/sec in the ion diamagnetic direction in the SOL. There but is a fairly consistent outward V_{rad} in the SOL of ~ 0.2 km/sec, but a slight reversal to an inward V_{rad} inside the separatrix.

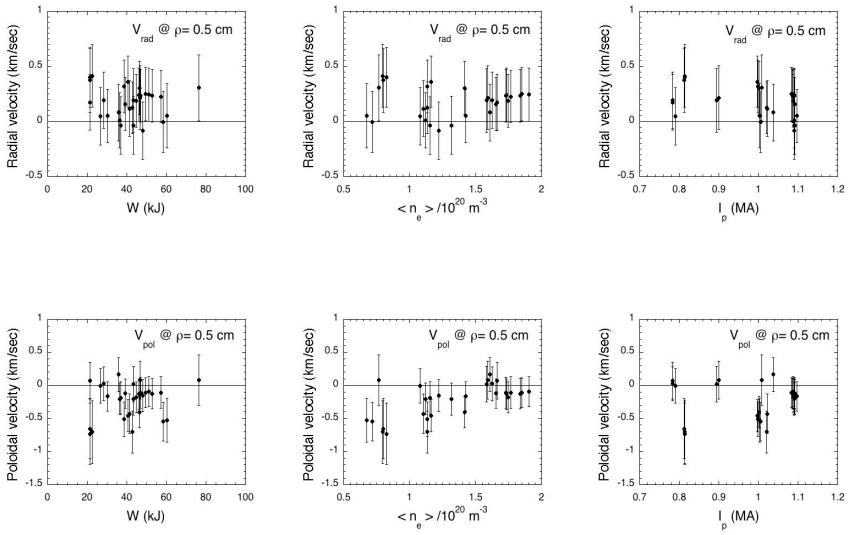

Fig. 7 – Poloidal and radial velocities at ρ=0.5 cm for the 30 shots in this database as a function of three global plasma parameters, W (stored energy), $<n_e>$ (line-averaged density), and I_p (plasma current). The RMS deviations from these average velocities are shown by the error bars. There is no clear variation in either the mean or RMS velocities with these parameters in this database.

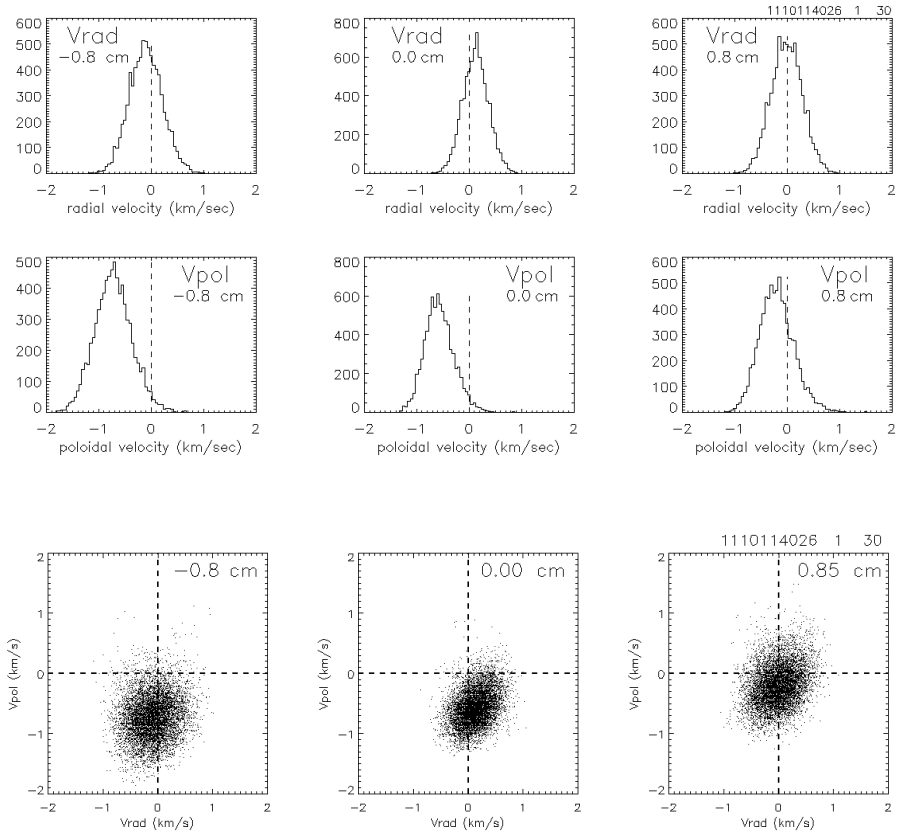

Fig. 8 - The top two panels show the probability distribution functions of V_{rad} and V_{pol} for three different radial locations in one shot (1110114026), averaged over 20 msec. The velocities have a large spread around their mean values in all cases. The bottom panel shows distributions of V_{rad} vs. V_{pol} for each time point for the cases above for the three different radial locations in 1110114026. There is a significant correlation between V_{rad} and V_{pol} at ρ= - 0.8 cm and ρ=0 cm.

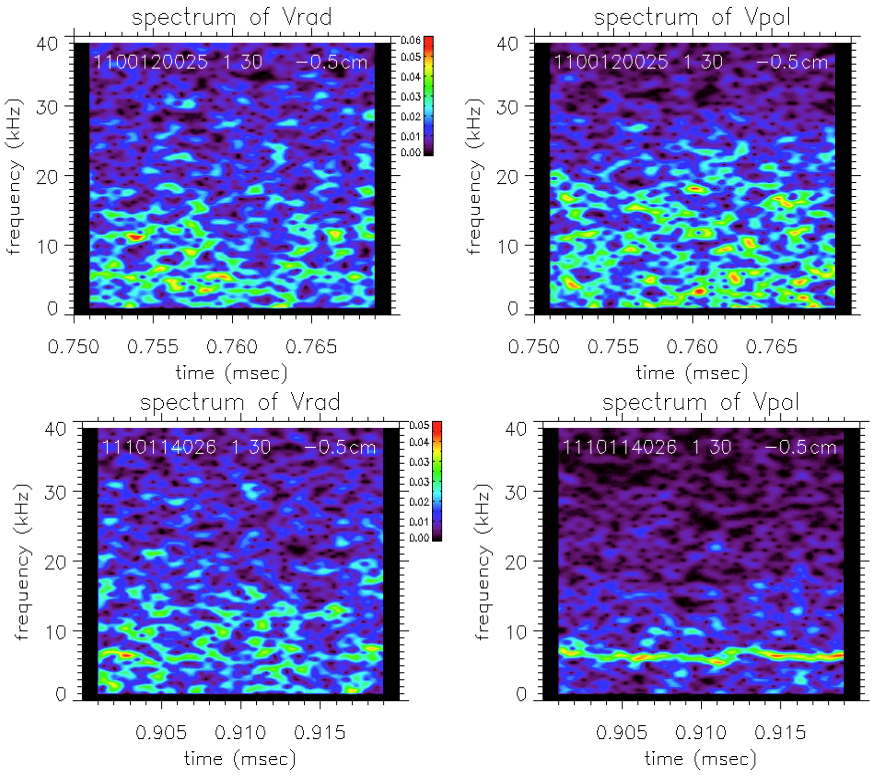

Fig. 9 – Examples of frequency spectra of V_{rad} and V_{pol} for ρ= - 0.5 cm for two shots (1100120025 and 1110114026). The amplitude spectrum of V_{pol} is broadband and intermittent for shot 100120025, but has a near-coherent component at 6-7 kHz for shot 1110114026. The V_{rad} do not have a clear coherent feature in the latter case.

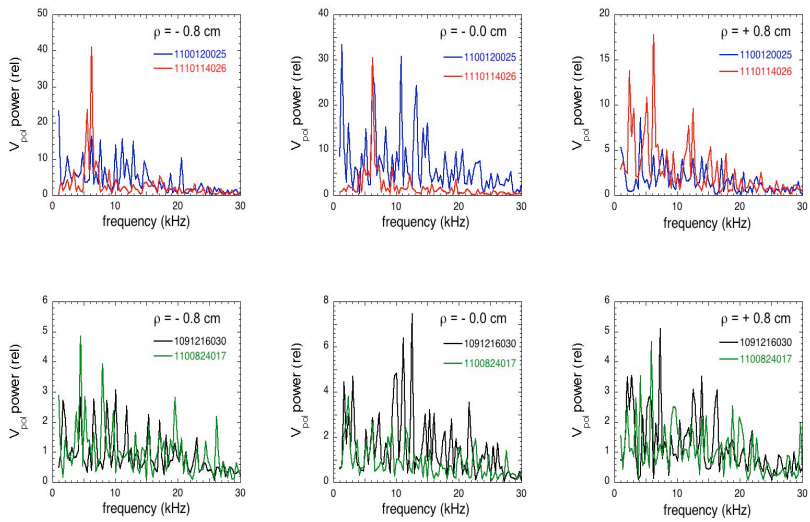

Fig. 10 – Frequency spectra of V_{pol} for the four typical shots of Fig. 6, for three different radii ρ = -0.8 cm, 0.0 cm, and +0.8 cm. These are power spectra averaged over 20 msec for each case. Note the varying vertical scales for each plot.

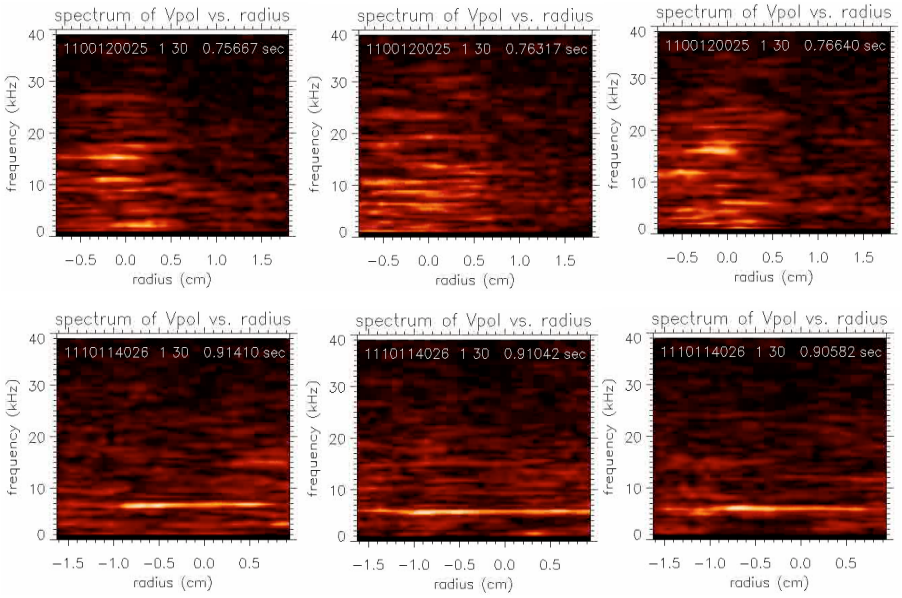

Fig. 11 – Radial profiles of frequency spectra of V_{pol} for three different times for the two shots of Figs. 9 and 10. For the top case (11000120025) the poloidal field fluctuations in the range ~1-20 kHz are mainly localized within ρ=±0.5 cm, but for the bottom case the near-coherent oscillation at 6-7 kHz is spread over at least ρ =±1 cm.

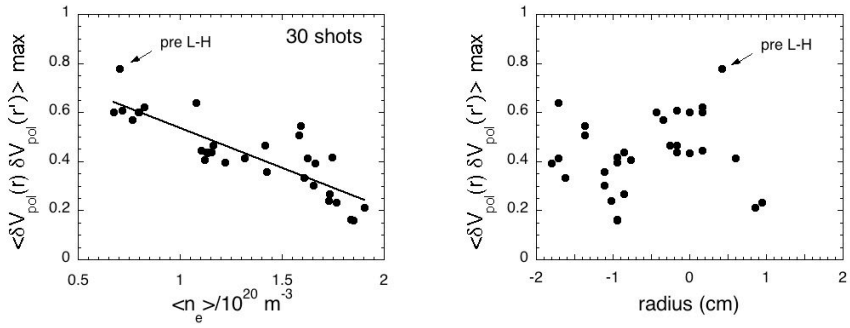

Fig. 12 – At the left is the maximum of the normalized cross-correlation coefficient $<\delta V_{pol}(r-\Delta/2)\ \delta V_{pol}(r+\Delta/2)>$, where Δ=0.35 cm, for all shots in Table 1. This correlation increases with decreased line-averaged density, and is largest for the 'pre-L-H' shot with a subsequent L-H transition (1110114032). The radius of this maximum cross-correlation coefficient is shown at the right.

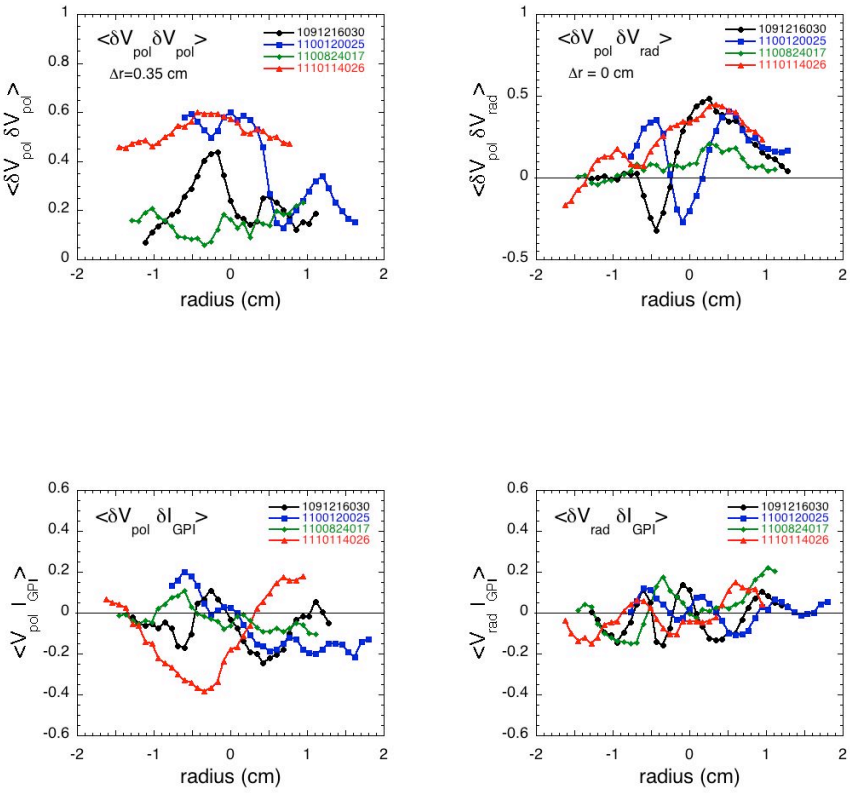

Fig. 13 – Normalized zero time delay cross-correlation coefficients of poloidal and radial velocity fluctuations with each other and with the GPI signal level fluctuations δI (averaged over the poloidal viewing region). At the upper left is $<\delta V_{pol}(r-\Delta/2)\ \delta V_{pol}(r+\Delta/2)>$, where Δ=0.35 cm. At the upper right is $<\delta V_{pol}(r)\ \delta V_{rad}(r)>$, which is related to the Reynolds' stress. At the bottom are $<\delta V_{pol}\ \delta I>$ and $<\delta V_{rad}\ \delta I>$, which are correlations of the poloidal velocity fluctuations with the GPI signal fluctuations.

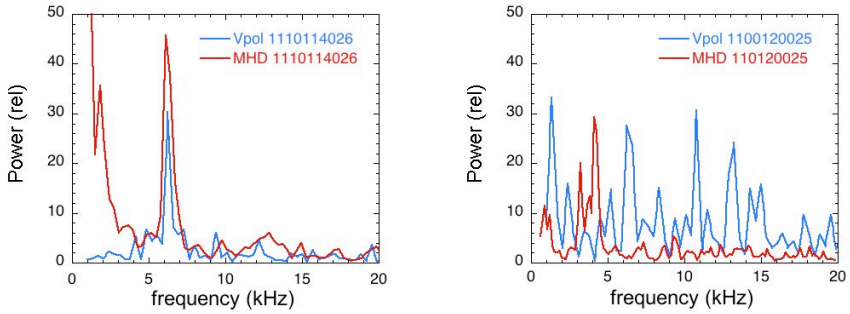

Fig. 14 – Comparison of the frequency spectra of V_{pol} at $\rho = 0$ cm for the two shots of Figs. 9 and 11 with the MHD spectrum from a B-dot coil at the wall, both averaged over 20 msec. There is a coincidence between the V_{pol} oscillation at 6-7 kHz and the MHD in the case at the left, but no correlation of these features in the case at the right.

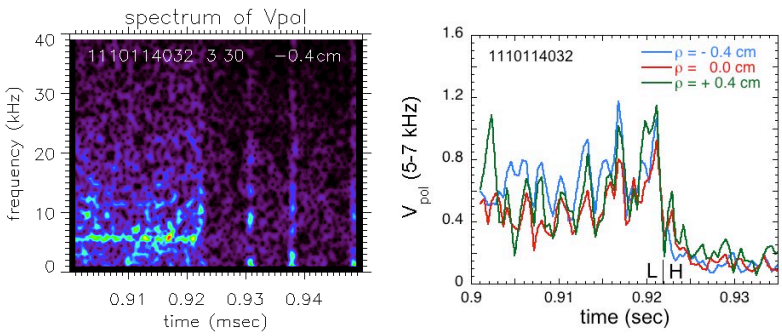

Fig. 15 – At the left is the V_{pol} spectrum vs. time of shot 1110114032 at ρ= -0.4 cm, showing a coherent oscillation at ~6 kHz which decreases in amplitude at the L-H transition at 0.923 sec. At the right is the V_{pol} magnitude vs. time within the frequency range 5-7 kHz for three radii for this shot, showing that the amplitude of the coherent oscillation decreases at the same time across over these radii, and that the ~0.5 kHz fluctuations preceding the L-H transition are common to all 3 radii.